nature astronomy

Article

https://doi.org/10.1038/s41550-024-02270-3

A unified framework for global auroral morphologies of different planets

Received: 19 July 2022

Accepted: 9 April 2024

Published online: 20 May 2024

Check for updates

B. Zhang[1], Z. Yao[1,2] ✉, O. J. Brambles[3], P. A. Delamere[4], W. Lotko[5,6], D. Grodent[7], B. Bonfond[7], J. Chen[1], K. A. Sorathia[8], V. G. Merkin[8] & J. G. Lyon[9]

Planetary magnetic fields control energetic particles in their space environments and guide particles to polar atmospheres, where they produce stunning auroral forms. As revealed by spacecraft measurements of the Earth, Saturn and Jupiter, the pathways of energetic particles to these planetary polar atmospheres are diverse, suggesting that there are different coupling processes between their ionospheres and magnetospheres. These planets all have dipole-dominated magnetic fields, rotate in the same direction and are blown by the solar wind, but what controls the global-scale patterns of energy dissipation remains unknown. Based on three-dimensional magnetohydrodynamics calculations, we reveal that the competition between planet-driven plasma rotation and solar-wind-driven flow convection determines the structure of global auroral morphologies. This unified theoretical framework can reproduce polar aurora from the Earth-type to the Jupiter-type based on transition states that are strikingly consistent with the highly variable aurora patterns of Saturn. This generalized description of fundamental magnetospheric physics, proposed here and validated by decades-long observations, is applicable to exoplanetary systems.

Planetary magnetic fields are generated by an electrically conducting fluid layer in their deep interiors through the dynamo process[1]. Within our Solar System, global magnetic fields are found around terrestrial planets, gas giants and an icy moon. Outside the Solar System, strong magnetic fields are also found around cool stars[2] and exoplanets such as rogue Jupiters[3]. Although they vary in tilt angle and intensity, all observed planetary magnetic fields have been shown to be primarily dipolar; however, all have unique anomalies that create distortions in the main field, which could be substantial near the planet surface. These planetary magnetic fields not only provide a window to infer the internal structure and dynamics of planets[4–8] but also act as a space laboratory for remote sensing the evolution of near-planet neutral and plasma environments[9–13].

Human spacecraft have visited all the planets in our Solar System and explored most of the planetary systems with dedicated space missions, except for Uranus and Neptune. The Earth, our homeland, has an atmosphere and a global magnetic field, resulting in a typical type of energy circulation and dissipation, as illustrated by the powerful auroral emission in polar regions[14,15]. Like the Earth, Saturn and Jupiter also have powerful polar auroral emissions[16,17], and thus, comparisons among these three planets are believed to be helpful for obtaining a universal picture of how particles and energy circulate in such planetary systems. It is well known that the terrestrial auroral emissions are generated by energetic particles precipitating along magnetic field lines[18,19], thus forming an auroral oval circling the magnetic pole (Fig. 1a). Although the magnetic fields of Saturn are also

[1]NWU-HKU Joint Centre of Earth and Planetary Sciences, Department of Earth Sciences, University of Hong Kong, Hong Kong SAR, China. [2]Institute of Geology and Geophysics, Chinese Academy of Sciences, Beijing, China. [3]Brambles Consulting, Preston, UK. [4]Geophysical Institute, University of Alaska Fairbanks, Fairbanks, AK, USA. [5]Thayer School of Engineering, Dartmouth College, Hanover, NH, USA. [6]National Center for Atmospheric Research, Boulder, CO, USA. [7]LPAP, Space Sciences, Technologies and Astrophysics Research (STAR), Institute Université de Liège (ULiége), Liège, Belgium. [8]Applied Physics Laboratory, Johns Hopkins University, Laurel, MD, USA. [9]Gamera Consulting, Hanover, NH, USA. ✉e-mail: yaozh@hku.hk

 https://doi.org/10.1038/s41550-024-02270-3

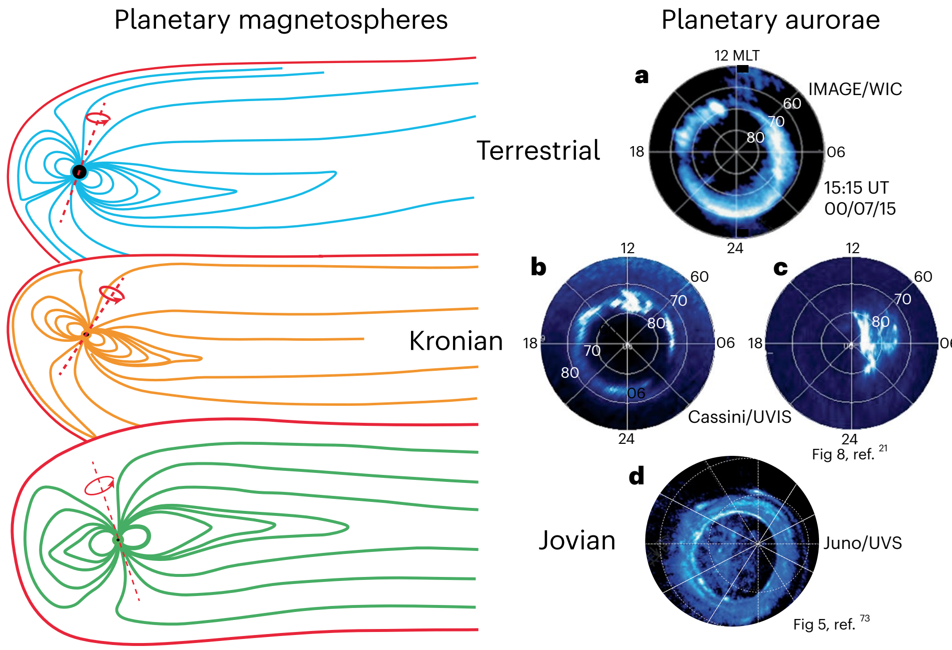

Fig. 1 | Variable Sun–planet magnetosphere interactions. a, Polar projections of the typical terrestrial auroral morphology from IMAGE FUV/WIC data. **b**,**c**, Saturn's dynamic auroral morphology observed by the ultraviolet imaging spectrograph (UVIS) on the Cassini–Huygens spacecraft (**b**) and by the Hubble Space Telescope (**c**)[21]. **d**, Jupiter's auroral morphology observed by the ultraviolet spectrograph (UVS) on the Juno orbiter[73].

dipole-dominated, their auroral emissions exhibit large variations with complicated morphologies[20–22], which resemble both Earth-like and Jupiter-like structures (Fig. 1b,c). The corresponding aurorae of Jupiter exhibit a completely different morphology and evolution[23–25] (Fig. 1d), including a highly dynamic—although generally bright—polar cap aurora and dark 'polar collar' regions. However, why are the morphologies of planetary aurorae so diverse even though the structures of their magnetic fields are similar? An answer to this question may not only explain the diverse planetary energy dissipations but also further our understanding of fundamental plasma processes at different spatial and temporal scales.

Results

Parameters controlling global auroral morphologies

From the fundamentals of plasma physics in magnetized environments, four potential ingredients are responsible for making the different auroral structures of the three planets: the upstream solar wind/interplanetary magnetic field (SW/IMF), the rotation speed of the planet, the strength of the planetary magnetic field and the mass-loading rate to the planetary system[26–28]. As shown in Table 1, these parameters are highly variable among the Earth, Saturn and Jupiter. The internal source is usually negligible in Earth's magnetosphere, but the ionospheric outflow rate during active times can be 1 kg s^{-1} (ref. 29), which is substantial for the magnetospheric structure considering that the volume of the Earth's magnetosphere is more than three orders of magnitude smaller than Saturn's or Jupiter's magnetospheres. As the motion of charged particles is controlled by electromagnetic fields, the first three parameters play pivotal roles as these are the main electromagnetic forcings of a planetary space environment[30]. Thus, to the first order, a working hypothesis is that the spatial distribution of polar energy dissipation of a planetary space system is determined by the competition between solar wind and rotating electric fields. If the electric field of the solar wind dominates the system dynamics, then the planetary system is defined as terrestrial-like from an auroral perspective[31] (Fig. 1a). In contrast, a system dominated by a rotating electric field is mostly Jovian-like[32] (Fig. 1d). Transient situations between these two extreme conditions are possibly Kronian-like[33] (Fig. 1b,c). Note that the rotating electric field is due to a combination of the planetary rotation speed and the magnetic field strength, that is, the second and third ingredients. As explained in Discussion, we could obtain a similar auroral evolution, that is, from terrestrial-like to Jovian-like, by increasing either the second or third term, which proves that the combination of both terms is the key factor.

Global-scale numerical simulations of the planetary magnetosphere systems were used in this study (Methods) to test the hypothesis on the controlling factor of planetary auroral morphology, given that global coverage of observations is limited for direct comparisons. These three-dimensional simulations are based on the theory of magnetohydrodynamics (MHD) and treat the space plasmas as magnetized fluids[34–40]. With the specification of proper upstream and low-altitude boundary conditions, the terrestrial magnetosphere was simulated, and the auroral morphologies were derived using electron precipitation models, validated by data-model comparisons[41]. To the first order in the understanding of the universal scaling law, we used an axisymmetric dipole magnetic field and ignored the effects of dipole tilt and the ionospheric conductance gradient in the magnetosphere-ionosphere coupling system (M-I system). The effects of mass loading were investigated by comparing two sets of simulations (that is, with and without mass loading). As the baseline case, we considered constant upstream conditions for the Earth's magnetosphere (that is, mainly antiparallel to the planetary fields and with a typical velocity of ~400 km s^{-1}, see the details in Table 1; ref. 31) with a corotating electric field corresponding to a full rotation every 24 h. For the super-rotating Earth cases, we increased the speed of Earth's rotation by a factor of 20, 50 or 100. These simulations show that the auroral morphology may evolve from one planetary type to another.

We chose the increase in the rotation speed used in the simulations based on the real situations of the Earth, Saturn and Jupiter using a simple dimensionless parameter R_{Φ}, calculated as the ratio of the merging potential of the solar wind (Φ_{merg}) to the corotation potential (Φ_{coro}) (Methods):

Table 1 | The SW/IMF and planetary parameters used in calculating the R_Φ values for the numerical experiment with increasing rotation speed

Parameter	Earth		Super-rotating Earth		Saturn	Jupiter
N_{SW} (cm^{-3})	5.0		5.0		0.1	0.2
U_{SW} (km s^{-1})	400		400		400	400
$\|B_{IMF}\|$ (nT)	2.0		2.0		0.5	1.0
θ_{IMF} (degree)	180		180		90	90
B_{Planet} (gauss)	0.31		0.31		0.21	4.17
Radius (R_{Planet})	1.0		1.0		9.9	11.2
T (h)	24.0 (baseline)	1.2 (×20)	0.48 (×50)	0.24 (×100)	11.0	9.9
L_{MP}	11	11	11	11	19	46
Φ_{recon} (kV)	89	89	89	89	250	718
Φ_{coro} (kV)	8.2	164	410	822	644	8232
R_Φ (Φ_{recon}/Φ_{coro})	10.8	0.54	0.22	0.11	0.38	0.09

The corresponding R_Φ values for Saturn and Jupiter were also calculated using the nominal SW/IMF parameters observed. N_{SW}, solar wind number density.

$$R_\Phi = \frac{\Phi_{merg}}{\Phi_{coro}} = \frac{2^{4/3} C_0 f^{2/3}}{\mu_0^{1/3} k^{1/3}} \frac{B_{SW}}{\Omega_{Planet} B_{Planet}^{2/3} R_{Planet}} \left(\frac{U_{SW}}{\rho_{SW}}\right)^{1/3}, \qquad (1)$$

where ρ_{SW} and U_{SW} are the mass density and velocity of the solar wind and B_{SW} is the strength of the IMF. Ω_{Planet}, B_{Planet} and R_{Planet} are the angular velocity, equatorial magnetic field strength and radius of the planet, respectively. μ_0 is the permeability of free space. C_0, f and k are empirical constants[42,43]. These empirical parameters were derived based on the terrestrial magnetosphere, and they work reasonably well for solar planets. Adjustments may be required when studying other stellar wind and magnetosphere interactions. The ratio R_Φ depends on both the planetary characteristics and the upstream SW/IMF conditions, but the dependence on an individual parameter is linear only for variations in IMF amplitude and planetary rotation period. As equation (1) does not make use of this assumption, it is a generally more useful indicator of the transition from a terrestrial magnetosphere to a rotation-dominated magnetosphere. Table 1 shows the value of R_Φ calculated for the super-rotating Earth cases compared to the baseline case, together with reference values calculated using nominal parameters for Saturn and Jupiter. In the super-rotating Earth experiments, the choices of the increased planet rotation cover a wide range of R_Φ (0.1–10). Note that the subsolar L shell of the magnetopause (L_{MP}) calculated for Jupiter using a one-dimensional pressure balance is lower than observations[44] as non-adiabatic plasma sources are not treated here.

The left-hand panels in Fig. 2 show the spatial distributions of the average z component of the magnetic field (B_z) in the equatorial plane, together with the open-to-closed boundary of the magnetic field separating the planetary magnetic fields from the IMF. The right-hand panels show the corresponding open magnetic flux region at ionospheric altitude. The numbered circles in the right-hand panels are mapped from the corresponding locations of the magnetic local time (MLT) in the equatorial magnetosphere, as indicated along the open-to-closed boundary in the left-hand panels. The MLT regions between 24 and 02 in the equatorial magnetosphere are coloured in purple in all panels to indicate the complicated field mapping, especially in the super-rotating cases. The magnetosphere open-to-closed boundary in purple is marked with the same colour in the ionospheric plots (right-hand panels). The red and blue plus signs in the left-hand panels are magnetically connected to the same-coloured markers in the right-hand panels. The colour shown in the right-hand panels indicates the field-aligned currents mapped to the ionospheric reference altitude (100 km), with blue for upward currents and red for downward currents. It is evident that as the planetary rotation speed was increased ×20 and above, the magnetic flux piled up near the dawn-side magnetopause due to the enhanced azimuthal transport of flux within the magnetosphere. This build-up is manifest as increased B_z and an elongated closed field line region in the dawn-side flank between 24 and 02 MLT. In these numerical experiments, the integrated reconnection rate on the dawn-side magnetopause remained approximately unchanged. Thus, magnetospheric flux tubes were transported into this region and cannot instantaneously open on the dawn flank. As a result, these flux tubes piled up on the dawn side. As the rotation speed was increased, the ionospheric mapping of this flux pile-up region moved towards the dayside near the pole at the ionospheric altitude, as indicated by the purple contours in the right-hand panels of Fig. 2. In the ×50 and ×100 cases, the pile-up of the open magnetic flux in the equatorial region between 24 and 02 MLT maps to the poleward edge of the open flux region. The global magnetic field configuration of the ×100 super-rotating Earth is like the real Jupiter simulation[45], and the magnetic connection between the dawn-side magnetosphere and dayside polar cap is supported by coherent in situ observations (for example, magnetic field and particles) and remote sensing X-ray aurorae[46]. This feature of a corotation-dominated magnetosphere–ionosphere differs radically from the prediction of a classic terrestrial magnetosphere with a completely open, disk-like polar cap.

Figure 3 shows the computed percentage of the magnetic flux above 80° magnetic latitude (MLAT) that is open as a function of the R_Φ parameter (Φ_{recon}/Φ_{coro}) defined in equation (1), as well as the corresponding spatial distribution of the Alfvénic oval[47,48], which is characterized by the downward Alfvénic Poynting flux at low altitude (Methods). In the baseline simulation driven by IMF $B_z = -2$ nT, the polar region was approximately 98% open above 80° MLAT, with a terrestrial Alfvénic oval circling the open flux boundary. This result resembles statistical observations[49]. Secondary effects not included in the simulations, such as the energized ring current, mass flux from the polar ionosphere and electrodynamic feedback from the upper atmosphere, will influence the fine detail of the power distribution. However, there is little doubt that the dominant factors determining the global structure are reconnection and corotation. As the planetary rotation speed was increased, R_Φ decreased and the motion of the lobe flux became increasingly azimuthal (in the direction of planetary rotation) rather than antisunward (in the direction of the solar wind), resulting in a more closed polar cap. As a result, the open magnetic flux above 80° MLAT decreased from 98% (the baseline) to approximately 24% (×100 case), and the simulated Alfvénic oval exhibited a striking similarity with the Jovian auroral emission as shown in Fig. 1d. The intermediate cases (×7, ×20 and ×50) show a clear transition of the Alfvénic oval from

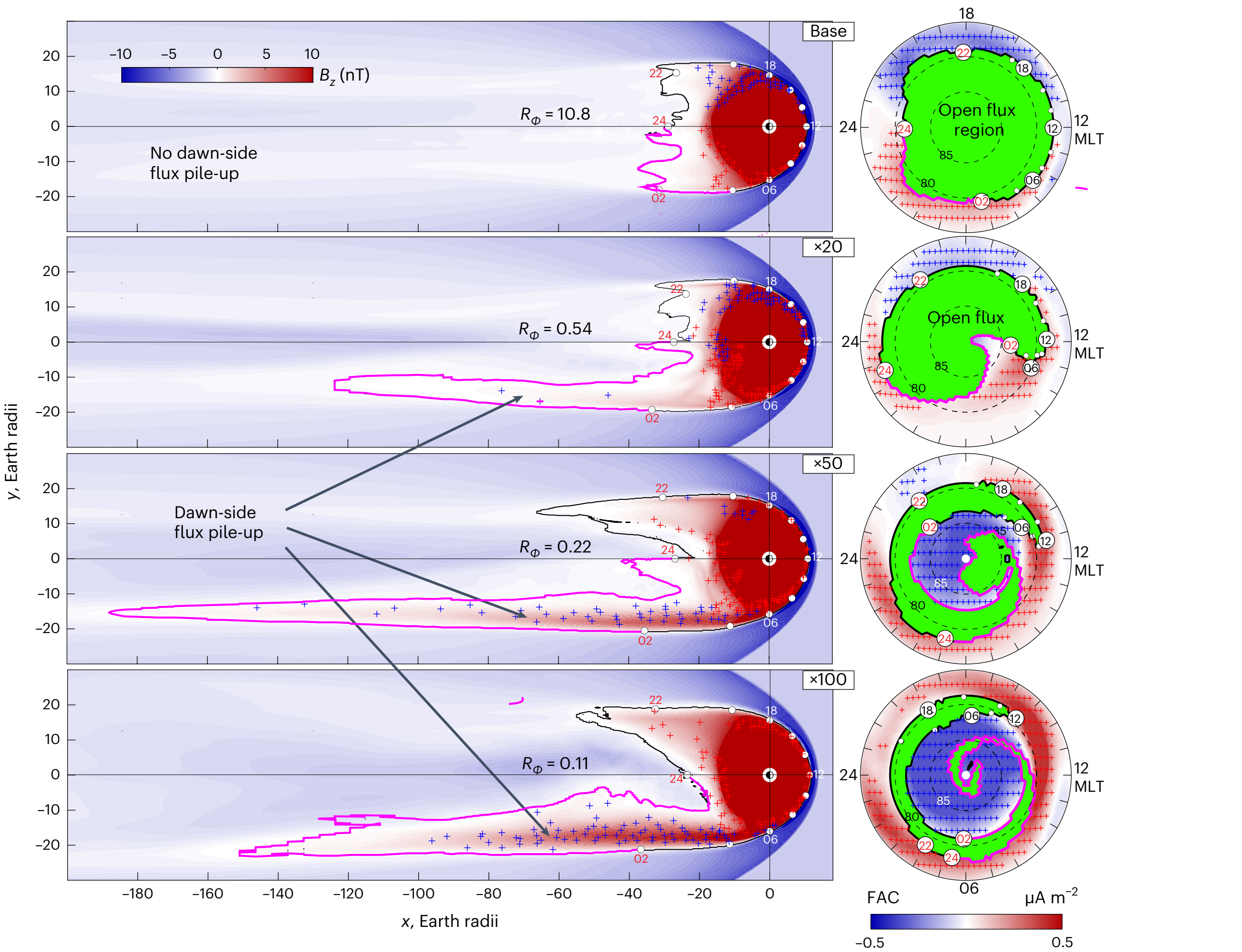

Fig. 2 | Magnetosphere–ionosphere connection. Left, spatial distributions of average B_z in the equatorial magnetosphere. The outlines indicate the contour $B_z = 0$, and the pink outlines are the boundaries post-midnight (local time ~0–2 h). Right, corresponding mapping of the open flux region in the ionosphere, with the labelled circles indicating the MLT location in the equatorial magnetosphere. The colour indicates the field-aligned currents (FAC) $j\cdot\mathbf{B}/B$ mapped to the ionospheric reference altitude (100 km). The pink outlines in the left-hand panels represent the flux pile-up region in the magnetosphere, and they correspond to the pink polar regions iun the right-hand panels. The green regions in the right-hand panels are open magnetic fields.

terrestrial-like to Jovian-like, with intense Alfvénic power deposition in the post-midnight sector, on the dawn side and in the noon sector, some of which also highly resemble the observed auroral emissions for Saturn (Fig. 1b,c). For comparison, we indicate on the plot typical R_Φ values for Saturn and Jupiter based on typically observed solar wind conditions[50,51] and rotation periods.

Discussion

These simulations demonstrate the transition from a terrestrial magnetosphere to a Jupiter-like magnetosphere. The transition between these extremes is gradual without a clearly defined transition point. The intermediate states exhibit mixed characteristics of terrestrial and Jovian magnetospheres. For a Jupiter-like planet, a 100% increase in R_Φ from 0.09 to 0.18 would be equivalent to a magnetosphere between the ×50 and ×100 cases, as listed in Table 1. Therefore, even accounting for second-order effects that are not considered in these simulations, Jupiter-like planets are probably firmly in the corotation-dominant regime when driven by non-extreme upstream conditions. These simulations suggest that Saturn-like planets are in the transitionary regime, exhibiting some terrestrial and some Jovian characteristics with the dominant regime dependent on solar wind driving, which is seen in the diverse auroral morphology. As indicated by equation (1), both the SW/IMF and planetary parameters contribute to R_Φ, which affects the morphology of the open flux. For example, a substantial increase in the magnitude of the IMF or speed of the solar wind may transition a Saturn-like magnetosphere from a corotation-dominated system to a terrestrial one. However, such a transition for a Jupiter-like planet is much harder and may require extreme solar wind conditions near the Jovian orbit. Note that the nonlinear response of the coupled SW-M-I system to the electric field of the solar wind includes effects that have been ignored in the simple form (1) used for the reconnection potential. Saturation of polar cap convection for large electric fields of the solar wind, feedback of ionospheric electrodynamics and increased erosion of the dayside magnetosphere all tend to reduce the effective reconnection potential and increase the effective R_Φ (refs. 52,53).

The importance of planetary rotation is quantified using the dimensionless parameter R_Φ, which is defined as the ratio of the merging potential to the corotation potential at the nominal location of the subsolar magnetopause. Planetary magnetospheres with $R_\Phi > 1$ follow the terrestrial case with a dark polar cap. For an R_Φ value of the order of 0.5, the planetary magnetosphere is regulated by both the merging of the solar wind and the planetary rotation, such that approximately 70% of the polar cap is open to the IMF. A Saturn-like magnetosphere (non-storm conditions) is in this parameter regime. That Saturn's auroral morphology sometimes resembles terrestrial aurorae indicates that its magnetosphere is largely controlled by the solar wind.

https://doi.org/10.1038/s41550-024-02270-3

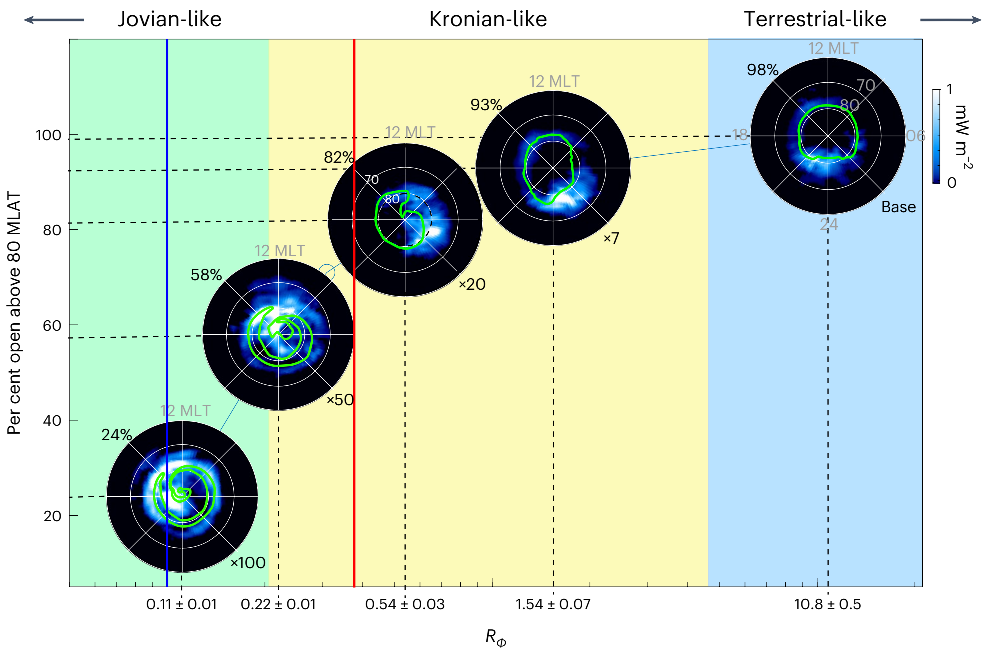

Fig. 3 | Variation of the simulated Alfvénic oval as a function of R_Φ. The percentage of the polar magnetosphere above 80° MLAT that is open is highly connected with R_ϕ and corresponds to different auroral morphologies. The blue and red lines denote R_ϕ for real Jupiter and Saturn using the nominal observed values of SW/IMF parameters listed in Table 1. The regions enclosed in the green outlines have open magnetic fields.

When R_Φ is of the order of 0.1, the Dungey cycle is insignificant compared to the rotation of the planet. The resulting polar cap is largely closed, with only about 20% of the polar magnetic flux open to the IMF. A Jupiter-like planet is firmly in this corotation-dominated regime, as supported by Jupiter's unique polar auroral morphology. We have considered only the effects of interplanetary driving combined with planetary rotation at various rates. Internal processes, such as mass loading[54], were found to change only the auroral energy distribution, but have little influence on the global morphology (Methods). We used the planetary size to scale down the mass-loading rate from the real Jupiter case to the super-rotating Earth, which represents a high mass-loading situation. Note that the mass-loading rate was not found to greatly influence auroral morphologies in previous literature[55]. We would like to point out that both the rotation speed and planetary magnetic strength play similar roles in driving the evolution of planetary auroral morphology. The comparisons between auroral morphologies for a super-rotating Earth and a slowly rotating planet with an intense magnetic field (Jupiter and Saturn) are detailed in Methods. Note that our model results are consistent with the rotational features of the main aurorae of Jupiter and Saturn, although the particle features (that is, acceleration[56] and pitch angle information) are beyond the capability of our model. A brief discussion related to the rotation of the current system can be found in Methods.

The numerical experiments performed in this study highlight the competing effects between the merging of the solar wind and planetary rotation in controlling the magnetic configuration of the planetary space environment. This first-order effect results in very different planetary space environments, including particle acceleration, mass circulation, and powerful auroral and radio emissions. Thus, the diverse auroral morphologies of the Earth, Saturn and Jupiter have been explained using this uniform framework. As more and more exoplanets with strong magnetic fields are discovered, the suggested uniform picture in this study could be widely applied to other star–planet systems[3].

Methods

Global magnetosphere simulation code

We used the Grid Agnostic MHD for Extended Research Applications (GAMERA) global model[57] to simulate the interaction of the solar wind and IMF with the terrestrial space environment, which is the volume of space where the geomagnetic field dominates the IMF. The model is based on the equations of single-fluid MHD (refs. 58,59), including: (1) a point dipole magnetic field embedded at the centre of the planet to represent the intrinsic magnetic field, (2) supersonic upwind conditions representing the solar wind and IMF to power the interaction, (3) low-altitude boundary conditions representing the closure of magnetospheric field-aligned currents in a thin-shell ionosphere and (4) rotation of the planet at the low-altitude boundary imposed through an electrostatic potential field.

The computational volume of the simulation was a stretched sphere of length 350 R_E along the x axis of the solar magnetic coordinate system of the Earth and 110 R_E in the directions perpendicular to the x axis. A spherical volume of radius 2 R_E was cut out from inside the distorted spherical computational domain. The sphere was centred on Earth, 30 R_E downstream from the upwind surface where the SW/IMF conditions are imposed. Supplementary Fig. 1 shows a three-dimensional view of the computational grid.

The primary computational technique was explicit, finite-volume MHD. The code used Adams–Bashforth time marching with an upwind, seventh-order, spatial reconstruction. In addition, nonlinear numerical switches based on the partial donor method were used to maintain the total variation diminishing property. A staggered grid was used to achieve zero numerical divergence of the magnetic field while fulfilling this total variation diminishing condition for the system of equations[60]. The finite-volume technique allowed the code to complete its calculation on a non-orthogonal numerical grid with cells adapted to the configuration of the terrestrial magnetosphere. For example, cells are smaller in the inner magnetosphere and across the nominal magnetopause than parallel to it. The computational grid used for the runs in this paper has 256 × 256 × 256 cells. The grid is spherical polar near the low-altitude boundary with an axis of symmetry along the solar magnetic x axis and with indices ($i \times j \times k$) corresponding approximately to the spherical ($r \times \theta \times \phi$) coordinates (radial × meridional × azimuthal) with horizontal resolution mapped to the ionosphere of approximately 0.5° × 0.5° in MLT and MLAT.

Numerical resistivity enabled magnetic reconnection in the code when and where the magnetic gradients reached the grid scale, which was approximately 0.1 R_E near the x line on the dayside magnetopause for the 256 × 256 × 256 resolution computational grid. The resulting reconnection electric field was typically of order $0.1v_A B_{in}$, in terms of the Alfvén speed v_A and magnetic field B_{in} in the reconnection inflow region. This practically universal scaling indicates that the reconnection rate was not caused by changes in numerical dissipation and that the numerical resistivity was simulating large-scale aspects of the reconnection appropriately[61]. It has also been shown that the global rate of dayside reconnection in the magnetosphere is controlled by upstream conditions in the global simulation model rather than the grid resolution of the simulation[62].

To simplify the analysis, we used an axisymmetric dipole magnetic field and ignored the effects of dipole tilt, ionospheric conductance gradient, and internal mass loading or escaping processes in the planetary system, focusing only on the first-order effect, which is the merging between the SW/IMF and the geomagnetic field with planetary rotation. For the simulation results discussed in the following sections, we preconditioned the magnetosphere by driving with the solar wind with southward IMF at −2 nT for 2 h, northwards (2 nT) for 2 h and then southwards at −2 nT for another 6 h to generate a well-established steady magnetosphere convection state for the controlled numerical experiments[55,63]. After the preconditioning period, the solar wind number density was set to 5 cm^{-3}, the velocity to 400 km s^{-1}, the speed of sound to 40 km s^{-1} and the IMF at B_z = −2 nT, with a uniform ionosphere Pedersen conductance 5 S (the Hall conductance is zero).

The desired corotation potential was applied at the ionosphere, which contributed to the total **E** × **B** drift velocity at the inner boundary. To simulate the Earth's magnetosphere (the baseline case), a corotation potential of 92 kV at 1 R_E at the equator represented a full rotation every 24 h (ref. 64). By increasing the magnitude of the corotation potential, we examined four additional cases with rotation speeds increased by a factor of 7, 20, 50 or 100, respectively. These numerical experiments are the super-rotating Earth cases. Each simulation with increased corotation was run for 20 full periods to ensure a quasi-steady state was reached. At this point, no major change in the magnitude or distribution of the field-aligned current was observed, and the magnetotail had reached a quasi-steady state without persistent changes in the tail dynamics or the field topology.

Derivation of R_Φ

Our choices for the increased rotation period were informed using a simple dimensionless parameter denoted R_Φ and calculated as the ratio of the merging potential of the solar wind (Φ_{recon}) to the corotation potential (Φ_{coro}). Many studies have been devoted to determining the merging potential for given interplanetary and geospace conditions (for example, ref. 65 and references therein). Any of these forms would serve our purpose. Any differences that changed the detailed profile of the amount of open polar flux versus R_Φ are presented later in this paper. We used a form derived from simple theoretical considerations that predicts global simulation results accurately except when the IMF direction (as defined below) is near 0° and the merging potential is small[61]:

$$\Phi_{recon} = 2C_0 B_{IMF} U_{SW} L_{MP} R_E \sin\frac{\theta_{IMF}}{2}, \quad (2)$$

where $C_0 \approx 0.8$ is an empirical constant, B_{IMF} is the magnitude of the IMF, U_{SW} is the speed of the solar wind, R_E is the radius of the Earth and θ_{IMF} is the clock angle of the IMF defined as atan(B_z/B_y). The parameter L_{MP} is the L value of the subsolar magnetopause location, which was calculated based on a one-dimensional pressure balance between the dynamic pressure of the solar wind and the magnetic pressure of the geomagnetic field[66]:

$$k\rho_{SW}U_{SW}^2 = \frac{(2fB_L)^2}{2\mu_0} = \frac{(2f)^2}{2\mu_0}\left(\frac{B_E}{L_{MP}^3}\right)^2, \quad (3)$$

where ρ_{SW} is the mass density of the solar wind, B_L is the strength of the geomagnetic field at the subsolar magnetopause and μ_0 is the permeability of free space. The parameters k and f are modifications to the pressure balance due to flow diversion and magnetic compression, respectively. For a hypersonic solar wind flow with γ = 5/3, the most probable values are k = 0.88 and f = 1.22 (ref. 42).

The corotation potential obtained by integrating the corotation electric field in the magnetic equatorial plane from infinity to the magnetopause is

$$\Phi_{coro} = \frac{1}{L_{MP}} B_E \Omega_E R_E^2. \quad (4)$$

Combining equations (2)–(4), the ratio between the merging potential and the corotation potential is calculated as:

$$R_\Phi = \frac{\Phi_{recon}}{\Phi_{coro}} = \frac{2^{4/3}C_0 f^{2/3}}{\mu_0^{1/3}k^{1/3}}\frac{B_{SW}}{\Omega_E B_E^{2/3} R_E}\left(\frac{u_{SW}}{\rho_{SW}}\right)^{1/3}. \quad (5)$$

Calculating the planetary Alfvénic oval

The Alfvénic oval is a very recent concept, which has been revealed in both observational and modelling studies. The term 'Alfvénic oval' evokes an analogy with the auroral oval, which was indeed the intention when it was first coined[48]. To reveal the Alfvénic oval, it is most convenient to map the Alfvén wave, measured in space, along magnetic field lines to the ionosphere. The Poynting flux associated with the magnetospheric Alfvén wave is the most common quantity to have been used for such mapping. Using the simulated electromagnetic fields, the Alfvénic Poynting flux is calculated from the perturbation electric (δ**E**) and magnetic (δ**B**) fields as:

$$S_{||} = \frac{1}{\mu_0}\delta\mathbf{E}\times\delta\mathbf{B}\cdot\frac{\mathbf{B}}{B}, \quad (6)$$

where μ_0 is the permeability of free space and **B** is the mean vector magnetic field, which is calculated from a 180 s running average of output results. Perturbation δ**E** and δ**B** were calculated by subtracting a 180 s running average of each field from the spurt value of per step (6 s). In the ionosphere, the resulting Poynting flux values were then projected to a reference ionospheric altitude of 100 km by mapping $S_{||}/B$ = constant along dipolar geomagnetic field lines. The downgoing fluxes of the full database of mapped $S_{||}$ values were then selected. These are analysed in the following section as a proxy for the wave auroral precipitation. The algorithm used for calculating $S_{||}$ in the simulation is shown in Supplementary Fig. 2.

Influences from internal mass loading

To investigate the influence of the internal mass-loading rate in driving auroral intensity and morphology, we performed six additional sets of numerical experiments with mass loading and compared the results with the results for no mass loading. To determine the amount of mass loading included in the numerical experiments, considering that the internal mass loading for Jupiter is about 1,000 kg s^{-1} and for Saturn is about 100 kg s^{-1}, we used the average amount ~1,000 kg s^{-1} to represent the maximum impact from an internal source. Note that the mass-loading rate is far from steady, as it may vary by several times[67,68]. As the simulations were based on the terrestrial magnetosphere, which has a volume that is approximately (R_E/R_J; R_J refers to Jupiter's radius, 1 R_J = 69,911 km) smaller[3], we used a mass-loading rate of ~1 kg s^{-1} in the simulations, which is a reasonable value scaled down to the size of the terrestrial magnetosphere. If the volume were scaled down using the magnetopause standoff distance, then the mass-loading rate would be much smaller, which was expected to be like the result with no mass loading. Therefore, the mass-loading rate ~1 kg s^{-1} represented a high mass-loading situation.

Supplementary Fig. 3 shows the 1 h average mass density in the equatorial plane together with the $B_z = 0$ contour to indicate the possible locations of x lines and o lines. The top panels are from the simulations without mass loading, and the lower panels show the simulation results from the mass-loading experiments. It is evident that the general morphology of the equatorial magnetosphere was not greatly influenced by the 1 kg s^{-1} mass loading added to the system, even though the inner magnetospheric density was as high as 300 AMU cm^{-3} near 4 R_E, suggesting that at least the dayside solar wind magnetosphere was less influenced by the torus mass added to the system. The results from these numerical experiments with a torus mass loading are consistent with the simulation results presented in ref. 55, in which a very intense outflow mass loading from the ionosphere was introduced in the terrestrial magnetosphere. Based on the numerical experiments in ref. 55, it is evident that for most of the parameter regime, the internal mass loading redistributed the dayside reconnection rates, whereas the integrated reconnection potential was largely determined by the solar wind[69]. Thus, in this study, our hypothesis for controlling the global morphology was based on the competition between the reconnection potential and rotation potential. The internal mass loading may have had a relatively small influence on R_Φ, as shown in the numerical experiments in Supplementary Fig. 3. However, under extreme situations (for example, mass loading greater than 128 AMU cm^{-3} at the magnetopause boundary[55]), the reconnection potential would be reduced by up to 50% and R_Φ would be expected to decrease, driving the system to become less terrestrial-like.

Supplementary Fig. 4 shows the 1 h average of the downward Alfvénic power, from simulations with and without mass loading. By adjusting the mass-loading rate in a rapidly rotating Earth model, we found that the mass-loading rate did not affect the global auroral morphologies. The rotation speed was the dominant factor. The key influence of the mass-loading rate would change the auroral energy distribution, but it had little influence on the global morphology. To conclude, from the comparisons among the 12 simulation sets, we found that mass loading affects the details of the Alfvénic oval, influences the intensity of the wave power, the thickness of the oval etc. but not the large-scale configuration associated with magnetic topology.

Simulated Alfvénic ovals of Jupiter and Saturn

Supplementary Fig. 5 compares the simulated Alfvénic ovals for the super-Earth case (×100) and the Jovian magnetosphere. The set-up for the simulation of the Jovian magnetosphere was taken from ref. 45, which was driven by nominal upstream SW/IMF conditions measured near the orbit of Jupiter. The Jovian oval was calculated using a band-pass filter of 60–1,800 s, which was calculated by scaling the terrestrial magnetosphere (6–180 s).

Supplementary Fig. 6 compares the simulated Alfvénic ovals for the super-Earth case (×20) and the Kronian magnetosphere. The simulation set-up is the same as in ref. 70, which was driven by nominal upstream SW/IMF conditions measured near the orbit of Saturn. The Alfvénic oval was calculated using a band-pass filter of 60–1,800 s (the same as in the Jovian magnetospheric simulation), which was calculated by scaling the terrestrial magnetosphere (6–180 s).

Simulated open flux and Alfvénic oval with different magnetic field strengths

To further confirm that R_ϕ could be controlled by varying the planetary magnetic field strength B_E rather than the planetary rotation frequency Ω_E alone, we performed an additional set of simulations, all with the same R_ϕ (0.11, the same as the ×100 case) but with different magnetic field strengths.

The left-hand panel of Supplementary Fig. 7 is a case with weaker dipole field strength ($0.5B_E$) but faster rotation speed ($150\Omega_E$), resulting in $R_\phi = 0.11$, as used in the ×100 case shown in the middle panel. The right-hand panel of Supplementary Fig. 7 is another case with a much stronger dipole field ($2.8B_E$) but slower rotation speed ($50\Omega_E$) compared to the ×100 case, which gives the same R_ϕ value as the middle panel. It is evident that in this set of numerical experiments, the simulated open-to-closed boundary and the average wave power exhibit the same morphology, with a mostly closed polar cap and substantial polar power. Note that due to the differences in the strength of the dipole field, the sizes of the simulated magnetosphere were different, resulting in latitudinal differences in the polar cap boundary and the auroral oval. However, the global morphology remained approximately the same when $R_\phi = 0.11$, as discussed. Note that the simulated distributions of average wave power are also consistent with the Jupiter simulation shown in Supplementary Fig. 5, which has an even stronger magnetic field ($15B_E$) but much slower rotation speed ($2.5\Omega_E$).

This set of simulations confirms our hypothesis that the parameter R_ϕ controls the first-order picture of planetary auroral morphology, regardless of whether R_ϕ is determined by the rotation speed alone or a combination of planetary and upstream conditions.

Corotating field-aligned current system

As we know, Jupiter and Saturn's Alfvén layers are both far beyond the magnetopause[71]. Therefore, the magnetospheric source regions driving the main aurorae are corotating with the planet. As a consequence of fast planetary rotation, the Alfvén layer naturally expands beyond the magnetopause, and therefore, the simulation indeed could reproduce well the corotating feature of the main aurorae of the giant planets[70,72]. Supplementary Fig. 8 is a keogram derived from the five sets of simulations, showing the variation of latitude-averaged (70–80 MLAT) intensity of $J_\parallel$ on the dawn side (0–12 MLT) as a function of time. The rotation speed of the planet is indicated use a dashed black line in each panel. It is clear that when the planetary rotation is increased, starting from ×7, the current system starts to rotate as the planet spins.

Data availability

The IMAGE FUV/WIC data, the UDF software for IMAGE data installation and FUVIEW3 for display were obtained from http://sprg.ssl.berkeley.edu/image/. The Hubble Space Telescope observations of Saturn's aurorae were obtained from https://archive.stsci.edu/hst/search.php, and the Jovian auroral image is archived in NASA's Planetary Data System (http://pds-atmospheres.nmsu.edu/data_and_services/atmospheres_data/JUNO/juno.html).

Code availability

The simulation data and source code are available upon request.

References

1. Jones, C. A. Planetary magnetic fields and fluid dynamos. *Annu. Rev. Fluid Mech.* **43**, 583–614 (2011).
2. Hallinan, G. et al. Magnetospherically driven optical and radio aurorae at the end of the stellar main sequence. *Nature* **523**, 568–571 (2015).
3. Kao, M. M., Hallinan, G., Pineda, J. S., Stevenson, D. & Burgasser, A. The strongest magnetic fields on the coolest brown dwarfs. *Astrophys. J. Suppl. Ser.* **237**, 25 (2018).
4. Stevenson, D. J. Interiors of the giant planets. *Annu. Rev. Earth Planet. Sci.* **10**, 257 (1982).
5. Stevenson, D. J. Planetary magnetic fields. *Earth Planet. Sci. Lett.* **208**, 1–11 (2003).
6. Guillot, T. The interiors of giant planets: models and outstanding questions. *Annu. Rev. Earth Planet. Sci.* **33**, 493–530 (2005).
7. Schubert, G. & Soderlund, K. M. Planetary magnetic fields: observations and models. *Phys. Earth Planet. Inter.* **187**, 92–108 (2011).
8. Liu, S., Kong, D. & Yan, J. Possible approach to detecting the mysterious Saturnian convective dynamo through gravitational sounding. *Astron. Astrophys.* **644**, A48 (2020).

9. Boakes, P. D. et al. On the use of IMAGE FUV for estimating the latitude of the open/closed magnetic field line boundary in the ionosphere. *Ann. Geophys.* **26**, 2759–2769 (2008).
10. Imber, S. M., Milan, S. E. & Hubert, B. The auroral and ionospheric flow signatures of dual lobe reconnection. *Ann. Geophys.* **24**, 3115–3129 (2006).
11. Fear, R. C. & Milan, S. E. The IMF dependence of the local time of transpolar arcs: implications for formation mechanism. *J. Geophys. Res.: Space Phys.* https://doi.org/10.1029/2011JA017209 (2012).
12. Milan, S. E., Lester, M., Cowley, S. W. H. & Brittnacher, M. Dayside convection and auroral morphology during an interval of northward interplanetary magnetic field. *Ann. Geophys.* **18**, 436–444 (2000).
13. Milan, S. E., Provan, G. & Hubert, B. Magnetic flux transport in the Dungey cycle: a survey of dayside and nightside reconnection rates. *J. Geophys. Res.: Space Phys.* https://doi.org/10.1029/2006JA011642 (2007).
14. Wing, S., Gkioulidou, M., Johnson, J. R., Newell, P. T. & Wang, C.-P. Auroral particle precipitation characterized by the substorm cycle. *J. Geophys. Res.: Space Phys.* **118**, 1022–1039 (2013).
15. Hardy, D. A., Gussenhoven, M. S. & Holeman, E. A statistical model of auroral electron precipitation. *J. Geophys. Res.: Space Phys.* **90**, 4229–4248 (1985).
16. Sandel, B. R. & Broadfoot, A. L. Morphology of Saturn's aurora. *Nature* **292**, 679–682 (1981).
17. Clarke, J. T. et al. in *Jupiter. The Planet, Satellites and Magnetosphere*, Vol. 1 (eds Bagenal, F. et al.) 639–670 (Cambridge Univ. Press, 2004).
18. Eather, R. H. & Mende, S. B. Airborne observations of auroral precipitation patterns. *J. Geophys. Res.* **76**, 1746–1755 (1971).
19. Eather, R. H. Auroral proton precipitation and hydrogen emissions. *Rev. Geophys.* **5**, 207–285 (1967).
20. Gérard, J.-C. et al. Saturn's auroral morphology and activity during quiet magnetospheric conditions. *J. Geophys. Res.: Space Phys.* **111**, A12210 (2006).
21. Grodent, D., Gérard, J.-C., Cowley, S. W. H., Bunce, E. J. & Clarke, J. T. Variable morphology of Saturn's southern ultraviolet aurora. *J. Geophys. Res.: Space Phys.* **110**, A07215 (2005).
22. Carbary, J. F. The morphology of Saturn's ultraviolet aurora. *J. Geophys. Res.: Space Phys.* **117**, A06210 (2012).
23. Clarke, J. T. in *Auroral Phenomenology and Magnetospheric Processes: Earth and Other Planets* (eds Keiling, A. et al.) 113–122 (AGU, 2012).
24. Greathouse, T. et al. Local time dependence of Jupiter's polar auroral emissions observed by Juno UVS. *J. Geophys. Res.: Planets* **126**, e2021JE006954 (2021).
25. Sulaiman, A. H. et al. Jupiter's low-altitude auroral zones: fields, particles, plasma waves, and density depletions. *J. Geophys. Res.: Space Phys.* **127**, e2022JA030334 (2022).
26. Hill, T. W. in *Solar-Terrestrial Physics: Principles and Theoretical Foundations* (eds R. L. Carovillano & J. M. Forbes) 261–302 (Springer, 1983).
27. Borovsky, J. E. The rudiments of a theory of solar wind/magnetosphere coupling derived from first principles. *J. Geophys. Res.: Space Phys.* https://doi.org/10.1029/2007JA012646 (2008).
28. Isbell, J., Dessler, A. J. & Waite, J. H. Jr. Magnetospheric energization by interaction between planetary spin and the solar wind. *J. Geophys. Res.: Space Phys.* **89**, 10716–10722 (1984).
29. Chappell, C. R., Moore, T. E. & Waite, J. H. Jr The ionosphere as a fully adequate source of plasma for the Earth's magnetosphere. *J. Geophys. Res.: Space Phys.* **92**, 5896–5910 (1987).
30. Delamere, P. A. et al. Solar wind and internally driven dynamics: influences on magnetodiscs and auroral responses. *Space Sci. Rev.* **187**, 51–97 (2015).
31. Russell, C. T. The solar wind interaction with the Earth's magnetosphere: a tutorial. *IEEE Trans. Plasma Sci.* **28**, 1818–1830 (2000).
32. McComas, D. J. & Bagenal, F. Jupiter: a fundamentally different magnetospheric interaction with the solar wind. *Geophys. Res. Lett.* https://doi.org/10.1029/2007GL031078 (2007).
33. Cowley, S. W. H. et al. Reconnection in a rotation-dominated magnetosphere and its relation to Saturn's auroral dynamics. *J. Geophys. Res.: Space Phys.* https://doi.org/10.1029/2004JA010796 (2005).
34. Leboeuf, J. N., Tajima, T., Kennel, C. F. & Dawson, J. M. Global simulation of the time-dependent magnetosphere. *Geophys. Res. Lett.* **5**, 609–612 (1978).
35. Lyon, J. G., Brecht, S. H., Huba, J. D., Fedder, J. A. & Palmadesso, P. J. Computer simulation of a geomagnetic substorm. *Phys. Rev. Lett.* **46**, 1038–1041 (1981).
36. Raeder, J., Berchem, J. & Ashour-Abdalla, M. The geospace environment modeling grand challenge: results from a global geospace circulation model. *J. Geophys. Res.: Space Phys.* **103**, 14787–14797 (1998).
37. Tanaka, T. The state transition model of the substorm onset. *J. Geophys. Res.: Space Phys.* **105**, 21081–21096 (2000).
38. White, W. et al. in *Space Weather* (eds Song. P. et al.) 229–240 (AGU, 2001).
39. Hu, Y. Q., Guo, X. C. & Wang, C. On the ionospheric and reconnection potentials of the Earth: results from global MHD simulations. *J. Geophys. Res.: Space Phys.* https://doi.org/10.1029/2006JA012145 (2007).
40. Janhunen, P., Koskinen, K. & Pulkinen, T. A new global ionosphere–magnetosphere coupling simulation utilizing locally varying time step. In Proc. International Conference on Substorms (eds Rolfe, E. J. and Kaldeich, B.) 205–210 (ESA, 1996).
41. Zhang, B., Lotko, W., Brambles, O., Wiltberger, M. & Lyon, J. Electron precipitation models in global magnetosphere simulations. *J. Geophys. Res.: Space Phys.* **120**, 1035–1056 (2015).
42. Choe, J. Y., Beard, D. B. & Sullivan, E. C. Precise calculation of the magnetosphere surface for a tilted dipole. *Planet. Space Sci.* **21**, 485–498 (1973).
43. Spreiter, J. R. & Alksne, A. Y. Plasma flow around the magnetosphere. *Rev. Geophys.* **7**, 11–50 (1969).
44. Joy, S. P. et al. Probabilistic models of the Jovian magnetopause and bow shock locations. *J. Geophys. Res.: Space Phys.* **107**, 1309 (2002).
45. Zhang, B. et al. How Jupiter's unusual magnetospheric topology structures its aurora. *Sci. Adv.* **7**, eabd1204 (2021).
46. Yao, Z. et al. Revealing the source of Jupiter's X-ray auroral flares. *Sci. Adv.* **7**, eabf0851 (2021).
47. Keiling, A., Wygant, J. R., Cattell, C. A., Mozer, F. S. & Russell, C. T. The global morphology of wave Poynting flux: powering the aurora. *Science* **299**, 383–386 (2003).
48. Keiling, A. The dynamics of the Alfvénic oval. *J. Atmos. Sol.-Terr. Phys.* **219**, 105616 (2021).
49. Zhang, B. et al. Magnetotail origins of auroral Alfvénic power. *J. Geophys. Res.: Space Phys.* https://doi.org/10.1029/2012JA017680 (2012).
50. Ebert, R., Bagenal, F., McComas, D. & Fowler, C. A survey of solar wind conditions at 5 au: a tool for interpreting solar wind-magnetosphere interactions at Jupiter. *Front. Astron. Space Sci.* **1**, 4 (2014).
51. Echer, E. Solar wind and interplanetary shock parameters near Saturn's orbit (~10 au). *Planet. Space Sci.* **165**, 210–220 (2019).
52. Merkin, V. G. et al. Global MHD simulations of the strongly driven magnetosphere: modeling of the transpolar potential saturation. *J. Geophys. Res.: Space Phys.* https://doi.org/10.1029/2004JA010993 (2005).

53. Siscoe, G., Raeder, J. & Ridley, A. J. Transpolar potential saturation models compared. *J. Geophys. Res.: Space Phys.* https://doi.org/10.1029/2003JA010318 (2004).
54. Hill, T. W. Inertial limit on corotation. *J. Geophys. Res.: Space Phys.* **84**, 6554–6558 (1979).
55. Zhang, B. et al. How does mass loading impact local versus global control on dayside reconnection? *Geophys. Res. Lett.* **43**, 1837–1844 (2016).
56. Salveter, A., Saur, J., Clark, G. & Mauk, B. H. Jovian auroral electron precipitation budget—a statistical analysis of diffuse, mono-energetic, and broadband auroral electron distributions. *J. Geophys. Res.: Space Phys.* **127**, e2021JA030224 (2022).
57. Zhang, B. Z. et al. GAMERA: a three-dimensional finite-volume MHD solver for non-orthogonal curvilinear geometries. *Astrophys. J. Suppl. Ser.* **244**, 35 (2019).
58. Brambles, O. J. et al. Magnetosphere sawtooth oscillations induced by ionospheric outflow. *Science* **332**, 1183–1186 (2011).
59. Wiltberger, M., Lotko, W., Lyon, J. G., Damiano, P. & Merkin, V. Influence of cusp O^+ outflow on magnetotail dynamics in a multifluid MHD model of the magnetosphere. *J. Geophys. Res.: Space Phys.* **115**, 7 (2010).
60. Lyon, J. G., Fedder, J. A. & Mobarry, C. M. The Lyon–Fedder–Mobarry (LFM) global MHD magnetospheric simulation code. *J. Atmos. Sol.-Terr. Phys.* **66**, 1333–1350 (2004).
61. Ouellette, J. E., Rogers, B. N., Wiltberger, M. & Lyon, J. G. Magnetic reconnection at the dayside magnetopause in global Lyon–Fedder–Mobarry simulations. *J. Geophys. Res.: Space Phys.* **115**, A08222 (2010).
62. Zhang, B. et al. Transition from global to local control of dayside reconnection from ionospheric-sourced mass loading. *J. Geophys. Res.: Space Phys.* **122**, 9474–9488 (2017).
63. Zhang, B., Brambles, O. J., Lotko, W. & Lyon, J. G. Is nightside outflow required to induce magnetospheric sawtooth oscillations. *Geophys. Res. Lett.* **47**, e2019GL086419 (2020).
64. Baumjohann, W. & Treumann, R. *Basic Space Plasma Physics* (World Scientific, 1996).
65. Burke, W. J., Weimer, D. R. & Maynard, N. C. Geoeffective interplanetary scale sizes derived from regression analysis of polar cap potentials. *J. Geophys. Res.: Space Phys.* **104**, 9989–9994 (1999).
66. Spreiter, J. R., Summers, A. L. & Alksne, A. Y. Hydromagnetic flow around the magnetosphere. *Planet. Space Sci.* **14**, 223–253 (1966).
67. Bagenal, F. & Delamere, P. A. Flow of mass and energy in the magnetospheres of Jupiter and Saturn. *J. Geophys. Res.: Space Phys.* https://doi.org/10.1029/2010JA016294 (2011).
68. Smith, H. T. et al. Enceladus plume variability and the neutral gas densities in Saturn's magnetosphere. *J. Geophys. Res.: Space Phys.* https://doi.org/10.1029/2009JA015184 (2010).
69. Lopez, R. E. The integrated dayside merging rate is controlled primarily by the solar wind. *J. Geophys. Res.: Space Phys.* **121**, 4435–4445 (2016).
70. Guo, R. L. et al. A rotating azimuthally distributed auroral current system on Saturn revealed by the Cassini spacecraft. *Astrophys. J. Lett.* **919**, L25 (2021).
71. Mauk, B. H. et al. in *Saturn from Cassini-Huygens* (eds Dougherty, M. K. et al.) 281–331 (Springer, 2009).
72. Palmaerts, B. et al. A long-lasting auroral spiral rotating around Saturn's pole. *Geophys. Res. Lett.* **47**, e2020GL088810 (2020).
73. Hue, V. et al. Detection and characterization of circular expanding UV-emissions observed in Jupiter's polar auroral regions. *J. Geophys. Res.: Space Phys.* **126**, e2020JA028971 (2021).

Acknowledgements

This work is supported by the Excellent Young Scientists Fund (Hong Kong and Macau) of the National Natural Science Foundation of China (Grant Nos. 41922060, 42074211 and 42374212) and Research Grants Council (RGC) General Research Fund (Grant Nos. 17308221, 17308520, 17315222 and 17308723).

Author contributions

B.Z. and Z. Y designed the numerical experiment and led the conceptual framework to understand the uniform auroral picture. O.J.B., J.C., K.A.S. and V.G.M. developed the numerical code. P.A.D., W.L. and J.G.L. provided crucial insights in the theoretical investigations. D.G. and B.B. processed the auroral images. All authors participated in producing the manuscript and revisions.

Competing interests

The authors declare no competing interests.

Additional information

Supplementary information The online version contains supplementary material available at https://doi.org/10.1038/s41550-024-02270-3.

Correspondence and requests for materials should be addressed to Z. Yao.

Peer review information *Nature Astronomy* thanks Robert Lysak and the other, anonymous, reviewer(s) for their contribution to the peer review of this work.